agriculture

MDPI

Article

CFNet: A Convolutional Fuzzy Network for Nondestructive Vigor Assessment of Naturally Aged Rice Seeds Using Hyperspectral Imaging

Shuqi Tang [1,2], Yuhao Zhou [1], Jinpeng Yang [1], Zequan Chen [1], Zijun Qin [1], Haochen Wu [1], Nan Zhong [1,3], Long Qi [4,5,*] and Xiao Feng [1,*]

[1] College of Engineering, South China Agricultural University, Guangzhou 510642, China; sqtang@stu.scau.edu.cn (S.T.); zhouyuhao@stu.scau.edu.cn (Y.Z.); yanggoldp@stu.scau.edu.cn (J.Y.); 15546787005@163.com (Z.C.); 202528110112@stu.scau.edu.cn (Z.Q.); 202528110319@stu.scau.edu.cn (H.W.); zhongnan@scau.edu.cn (N.Z.)
[2] Food, Nutrition and Health, Faculty of Land and Food Systems, The University of British Columbia, Vancouver, BC V6T 1Z4, Canada
[3] School of Intelligent Manufacturing and Equipment, Guangdong Communication Polytechnic, Guangzhou 510650, China
[4] College of Water Conservancy and Civil Engineering, South China Agricultural University, Guangzhou 510642, China
[5] Department of Biosystems Engineering, University of Manitoba, Winnipeg, MB R3T 5V6, Canada
* Correspondence: qilong@scau.edu.cn (L.Q.); fengxiao@scau.edu.cn (X.F.)

Abstract

Accurate, non-destructive assessment of rice seed vigor is challenging because natural aging causes gradual and heterogeneous deterioration. Although hyperspectral imaging offers a means of assessing vigor, overlapping spectral responses between vigor classes complicate their discrimination. To address this ambiguity, this study proposed a Convolutional Fuzzy Network (CFNet) that integrates one-dimensional convolutional feature extraction with fuzzy membership-based representation to model uncertainty near class boundaries. Naturally aged rice seeds from Huahang 31 (HH31) and Meixiangzhan 2 (MXZ2) were imaged using visible–near-infrared (VNIR, 397.66–1003.81 nm) and short-wave infrared (SWIR, 935.61–1720.23 nm) hyperspectral systems, and seed vigor was labeled using a Seed Vigor Index derived from germination and early growth traits. CFNet was evaluated against partial least squares discriminant analysis (PLS-DA), support vector machine (SVM), and one-dimensional convolutional neural network (1D-CNN) models. It achieved the best performance among the evaluated models, with 90.95% accuracy and 90.29% F1-score for HH31 in SWIR, and 87.14% accuracy and 85.96% F1-score for MXZ2 in VNIR. Ablation and t-SNE analyses showed that the standalone contribution of the fuzzy branch was condition-dependent, while its fusion with CNN features provided complementary soft-boundary information. Grad-CAM++ further revealed class-discriminative wavelength regions associated with aging-related physiological changes. These results indicate that CFNet provides an interpretable and robust framework for non-destructive vigor screening of naturally aged rice seeds.

Keywords: rice seed vigor; natural aging; hyperspectral imaging; CFNet; interpretability

Check for updates

Academic Editor: Petr Smýkal

Received: 4 November 2026
Revised: 22 November 2026
Accepted: 26 November 2026
Published: 29 November 2026

Copyright: © 2026 by the authors. Licensee MDPI, Basel, Switzerland. This article is an open access article distributed under the terms and conditions of the Creative Commons Attribution (CC BY) license.

1. Introduction

Rice (*Oryza sativa* L.) is one of the world's most important staple crops and a fundamental agricultural raw material supporting global crop production [1–3]. Under increasing pressures from climate extremes, geopolitical instability, and economic uncertainty, the reliability of agricultural production systems has become progressively more dependent on the availability of high-quality seeds capable of stable field establishment [4]. Among various seed quality attributes, seed vigor is widely recognized as a comprehensive indicator that governs not only germination capacity but also germination speed, emergence uniformity, seedling stress tolerance, and early field establishment, thereby exerting a decisive influence on crop yield formation and grain quality [5].

Despite its agronomic importance, seed vigor assessment in routine practice still relies predominantly on conventional methods such as standard germination tests, electrical conductivity (EC) measurements, and tetrazolium (TZ) staining [6]. These approaches are inherently destructive, labor-intensive, and time-consuming, making them poorly suited for large-scale screening or real-time decision-making in modern seed production and storage systems [7]. Consequently, there is a growing demand for non-destructive, rapid, and reliable techniques capable of assessing seed vigor at the individual-seed level.

With advances in spectral sensing and artificial intelligence, hyperspectral imaging (HSI) combined with machine learning has been widely explored as a non-destructive tool for seed quality evaluation [8,9]. By simultaneously capturing spatial morphology and continuous spectral responses, HSI enables indirect characterization of both external phenotypes and internal biochemical variations associated with seed deterioration [10]. Accordingly, HSI has been successfully applied to a range of seed-related tasks, including viability assessment [11], variety identification [12], pathogen detection [13], and insect damage detection [14]. In the context of seed vigor evaluation, numerous studies have reported high classification accuracy by coupling HSI with machine learning or deep learning models. For instance, Wu et al. addressed class imbalance using a weighted-loss deep convolutional neural network and achieved 97.69% accuracy for vigor classification under controlled experimental conditions [15]. Zhang et al. simulated heat damage through controlled drying and demonstrated that HSI combined with spectral preprocessing and conventional classifiers could reliably distinguish heat-damaged rice seeds [16]. Similarly, He et al. reported that compact band sets derived from NIR-HSI achieved comparable performance to full-spectrum models when differentiating seeds from different harvest years [17]. Jin et al. further extended HSI-based modeling to naturally aged rice seeds, reporting classification accuracies exceeding 85% using CNN, SVM, and logistic regression models [18]. Despite these encouraging results, a closer examination reveals that most existing HSI-based vigor studies implicitly rely on experimental settings where seed deterioration occurs in discrete or synchronized stages, such as accelerated aging treatments or clear storage-year separation. Under these conditions, vigor loss is artificially intensified, and spectral differences between classes are amplified, leading to well-separated feature distributions that favor hard-boundary classifiers. However, natural aging during real storage is governed by fluctuating environmental factors, resulting in gradual, heterogeneous, and individual-specific deterioration trajectories [19]. Consequently, vigor-related spectral signatures exhibit substantial overlap and smooth transitions rather than forming clearly separable clusters. This mismatch highlights a fundamental limitation of existing approaches: methods that perform well under artificially induced or discretized aging conditions are not necessarily suitable for modeling naturally aged seeds, where vigor degradation follows a continuous process rather than a binary or multi-stage pattern. Moreover, seed vigor itself is a compound trait encompassing germination probability, speed, uniformity, and post-germination growth potential, which cannot be fully represented by

germination outcome or storage duration alone [18,20,21]. Treating vigor identification under natural aging as a conventional classification problem therefore risks imposing artificial decision boundaries on intrinsically ambiguous physiological states.

From a modeling perspective, CNN-based classifiers can map one-dimensional signals to discrete classes [22]. Assigning seeds to discrete vigor classes can be straightforward when controlled aging treatments produce distinct levels of deterioration. During natural storage, however, seed vigor can decline gradually and at different rates among individual seeds. Applying a fixed cutoff to the seed vigor index can assign seeds with similar spectra to different classes, making samples near the cutoff difficult to distinguish. Similar difficulties arise in the grading of other agricultural products. In crude tea grading, for example, subtle differences in chemical composition and appearance can result in overlapping spectra and similar images across grades. Li et al. [23] addressed this problem by incorporating fuzzy operations into the image branch of their spectrum–image fusion network. In spectroscopy, Gong et al. [24] combined fuzzy and neural features from elemental images and point spectra to address fluctuations in laser-induced breakdown spectroscopy (LIBS). Fuzzy logic uses degrees of membership to represent graded properties [25]. For naturally aged rice seeds, the gradual changes in vigor motivate a feature representation that can respond continuously to small spectral differences. Based on this observation, we propose a Convolutional-Fuzzy Network (CFNet) that processes the same reflectance spectrum through two parallel branches. The 1D CNN extracts local spectral features, and the fuzzy branch applies Gaussian membership functions to downsampled spectral nodes. A learned gate weights the two feature vectors for each seed before fusion and vigor classification.

This study is based on the hypothesis that rice seed vigor identification under natural aging constitutes an intrinsically soft-boundary learning problem, where gradual physiological deterioration and individual heterogeneity lead to overlapping and ambiguous spectral signatures. Under such conditions, preserving uncertainty and spectral continuity is essential for stable and biologically plausible modeling. To examine this hypothesis, visible–near-infrared (VNIR) and short-wave infrared (SWIR) hyperspectral data were collected from two rice cultivars subjected to different levels of natural aging. Seed vigor was characterized using a comprehensive Seed Vigor Index (SVI) derived from germination behavior and post-germination growth traits. CFNet was then developed to relax hard assignment assumptions in hyperspectral feature learning and evaluated against conventional models. In addition, Grad-CAM++ was employed for spectral interpretation, and a prototype online detection platform was implemented to demonstrate practical applicability.

2. Materials and Methods

2.1. Sample Preparation

In this study, naturally aged seeds from two rice cultivars, Huahang 31 (HH31) and Meixiangzhan 2 (MXZ2), were used. The seeds were collected from the Teaching and Research Base of South China Agricultural University (Guangzhou, Guangdong, China) and harvested in November 2023, July 2024, and November 2024. All samples were threshed using a small electric threshing machine and stored under conventional warehouse conditions to simulate storage environments closely resembling actual agricultural practices during natural aging. During sample selection, seeds with visible mold, insect damage, or apparent physical defects were excluded to ensure the stability and representativeness of the experimental data. Detailed information is provided in Table 1.

Table 1. Rice seed information.

Variety Name	Year Code	Harvest Time	Sample Size	Remarks
HH31	2023II	2023.11	350	Production site: Teaching and Research Base of South China Agricultural University (Guangzhou) Harvest method: Small electric motor rice thresher Storage method: Standard storage conditions
	2024I	2024.07	350	
	2024II	2024.11	350	
MXZ2	2023II	2023.11	350	
	2024I	2024.07	350	
	2024II	2024.11	350	

2.2. Hyperspectral Imaging System and Spectral Data Acquisition

In this study, two HSI systems were employed: a visible–near-infrared system (VNIR-HSI, spectral range: 397.66–1003.81 nm) and a short-wave near-infrared system (SWIR-HSI, spectral range: 935.61–1720.23 nm). Both systems shared the same working platform, as illustrated in Figure 1. The setup included a dark chamber, two hyperspectral cameras (Specim FX10 and Specim FX17, Specim, Spectral Imaging Ltd., Oulu, Finland), a 280 W halogen light source (DECOSTAR 51S, Osram, Munich, Germany), a motorized translation stage (HXY-OFX01, Red Star Yang Technology Corp., Wuhan, China), and image acquisition software (Lumo-Scanner). The detailed parameters of both systems are listed in Table 2.

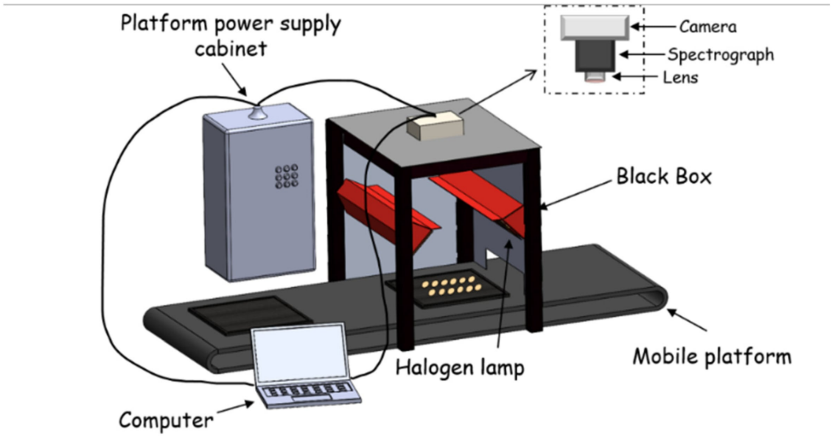


Figure 1. Hyperspectral imaging system.

Table 2. System Parameters of VNIR-HSI and SWIR-HSI.

System	Platform Speed	Exposure Time	Lens-Sample Distance	Spectral Resolution
VNIR-HSI	9.8 mm/s	2 ms	32 cm	2.68 nm
SWIR-HSI	7.5 mm/s	3.2 ms	32 cm	1.68 nm

Before hyperspectral image acquisition, the system was preheated for 30 min to ensure imaging stability. A black reference image (I_B) and a white reference image (I_W) were then collected to eliminate errors caused by fluctuations in light source intensity and dark current noise. After image acquisition, the raw images were corrected using I_B and I_W according to the calibration algorithm shown in Equation (1):

$$R_c = \frac{R_{raw} - I_B}{I_W - I_B} \quad (1)$$

where R_c is the calibrated reflectance image and R_{raw} is the raw image.

During data acquisition, the 350 seeds in each cultivar–harvest-year group were imaged in seven separate batches of 50 seeds. For each batch, the seeds were evenly placed on a black background board without touching one another and scanned using both the VNIR

and SWIR systems. A total of 84 hyperspectral images were acquired, comprising 42 VNIR images and 42 SWIR images of the same 2100 seeds (1050 HH31 and 1050 MXZ2). Threshold-based masking was then applied to remove the background and segment individual seeds, and the mean spectrum was extracted from each seed region. Each seed's spectrum was matched to the germination and seedling-growth records of that same seed, which were used to calculate its SVI and assign its reference vigor label.

Finally, to maintain comparable harvest-year and vigor-class distributions among subsets, samples were first stratified by harvest year and vigor status and then divided into training (60%), validation (20%), and test (20%) sets using the Kennard–Stone (K–S) algorithm. The training set was used to optimize model parameters, the validation set was used to select model weights, and the selected model was subsequently evaluated on the test set.

2.3. Germination Test and Seed Vigor Assessment Standards

After hyperspectral imaging, germination tests were performed for each cultivar–harvest-year group. Fourteen trays were used per group, with 25 seeds placed in each tray, giving 350 seeds per group. The three groups therefore comprised 1050 seeds per cultivar and 2100 seeds in total for both cultivars. Seeds were randomly assigned to trays and placed on moistened filter paper. Each seed received an identification code indicating its cultivar, harvest-year group, tray number, and position in the tray. The trays were incubated for 7 days in a growth chamber (GYJ-260B, Gongyouji Industrial Technology, Shenzhen, China) at 30 °C and 80 ± 2% relative humidity. Germination conditions were set at 30 °C and 80 ± 2% relative humidity for a period of 7 days. During the experiment, germination progress was monitored daily, including the time of seed coat rupture and the date of germination. At the end of the experiment, the final growth status of each seed was recorded, including whether it had germinated, radicle length (in cm), radicle fresh weight (in g), shoot length (in cm), and shoot fresh weight (in g). The overall germination rate was then calculated. According to the criteria of the International Seed Testing Association (ISTA), seeds with radicles of at least 2 mm in length were considered germinated.

In previous studies, seed vigor was often evaluated only by germination occurrence. However, germination alone does not fully reflect vigor, as some seeds may germinate but fail to develop into seedlings. To achieve a more accurate assessment, in this study, an individual-seed vigor index (SVI) was adapted from the maize seed assessment framework proposed by Zhu et al. [26]. In their method, germination potential was scored according to seed rupture stages observed at 48 h. However, a fixed assessment at 48 h may assign a zero germination score to delayed-germinating seeds that retain subsequent seedling growth potential. To account for this possibility in naturally aged rice seeds, we replaced the original germination-potential score with a germination-time score (SGP). This modification allowed delayed-germinating seeds to receive nonzero scores while retaining higher scores for earlier germination. Specifically, SGP was assigned as 1.0 for germination within 48 h, 0.5 for germination after 48 h and within 72 h, 0.2 for germination after 72 h and within 96 h, and 0 for seeds that had not germinated by 96 h. The SVI was calculated using Equation (2):

$$SVI = 0.6 \times SGP + 0.1 \times (PRL + PRW + SL + SW) \quad (2)$$

Here, PRL, PRW, SL, and SW denote primary root length, primary root fresh weight, shoot length, and shoot fresh weight, respectively. These traits were measured at the end of the 7-day germination test and normalized to a range of 0–1 separately for each cultivar. Following Zhu et al. [26], SGP was assigned a weight of 0.6, while each of the four growth traits was assigned a weight of 0.1. The SVI cutoff of 0.4 was also retained from this framework. Because the four normalized growth traits together contribute a maximum of

0.4, exceeding this cutoff requires a nonzero contribution from the germination score. This criterion emphasizes germination timing alongside subsequent seedling growth. Seeds were classified as high-vigor (SVI > 0.4), low-vigor ($0 < \text{SVI} \leq 0.4$), or non-vigorous (SVI = 0). For binary classification, high-vigor seeds were assigned label 1, whereas low-vigor and non-vigorous seeds were combined and assigned label 0.

2.4. Determination of CAT, MDA, and SOD

To evaluate the oxidative status of rice seeds under different natural aging stages, catalase (CAT) activity, malondialdehyde (MDA) content, and superoxide dismutase (SOD) activity were determined [19]. All assays were conducted using commercial kits (CAT: Servicebio G4307; MDA: Servicebio G4302; SOD: Servicebio G4306, Wuhan Servicebio Technology Co., Ltd., Wuhan, China) according to the manufacturer's instructions. For each aging stage, 10 biological replicates were prepared for each indicator, and each replicate consisted of three pooled seeds. Samples were homogenized in pre-cooled extraction buffer (1:9, w/v) on ice, centrifuged at 10,000× g for 10 min at 4 °C, and the supernatant was collected for analysis. Protein concentration was determined using the BCA method and used for normalization of enzyme activities and metabolite contents.

2.5. Scanning Electron Microscopy (SEM) Observation of Starch Granules

After dehulling, rice seeds were manually split longitudinally into halves, and both ends were trimmed with a scalpel to obtain flat surfaces for stable mounting on the specimen stage. The samples were then coated with a gold–palladium alloy for approximately 50 s using an ion sputter coater under vacuum conditions. Subsequently, the morphology and surface microstructure of endosperm starch granules were observed and imaged using a ZEISS G300 scanning electron microscope (Carl Zeiss Microscopy GmbH, Oberkochen, Germany) operated at an accelerating voltage of 2 kV.

2.6. Model Structure and Evaluation Metrics

2.6.1. Convolutional-Fuzzy Network

(1) CNN branch

To extract locally discriminative features from the spectral sequence, CFNet incorporates a one-dimensional convolutional branch, as illustrated in Figure 2a. This branch takes a spectral vector of length 224 as input and processes it through three convolutional modules, each consisting of a convolution layer, batch normalization, ReLU activation, and max-pooling. The first convolutional layer employs a relatively large kernel (9×1) to capture the overall spectral trend, while the subsequent layers use smaller kernels (7×1 and 5×1) to extract local band characteristics and subtle variations. The resulting feature maps are flattened and passed through a fully connected layer ($3328 \rightarrow 128$) with dropout regularization ($r = 0.2$) to mitigate overfitting. The final 128-dimensional feature vector effectively encodes local spectral variations and discriminative information, providing complementary features to the fuzzy membership branch.

(2) Fuzzy branch

As illustrated in Figure 2b, the 224-dimensional spectral vector $S_{224} = (s_1, s_2, \ldots, s_{224})$ is used as the input. To reduce computational complexity and capture local spectral-domain patterns, a one-dimensional convolutional layer ($Conv1D$) with both kernel size and stride set to 7 is first applied for sequence downsampling along the spectral axis:

$$C = Conv1D(S) \tag{3}$$

The output dimension is thereby reduced from the original 224 to 32 spectral nodes, i.e.,

$$S_{224} \rightarrow C_{32} = (c_1, c_2, \ldots, c_n) \tag{4}$$

In this process, each convolution kernel integrates the local information from seven adjacent bands, thereby reducing input redundancy while preserving the principal spectral response features.

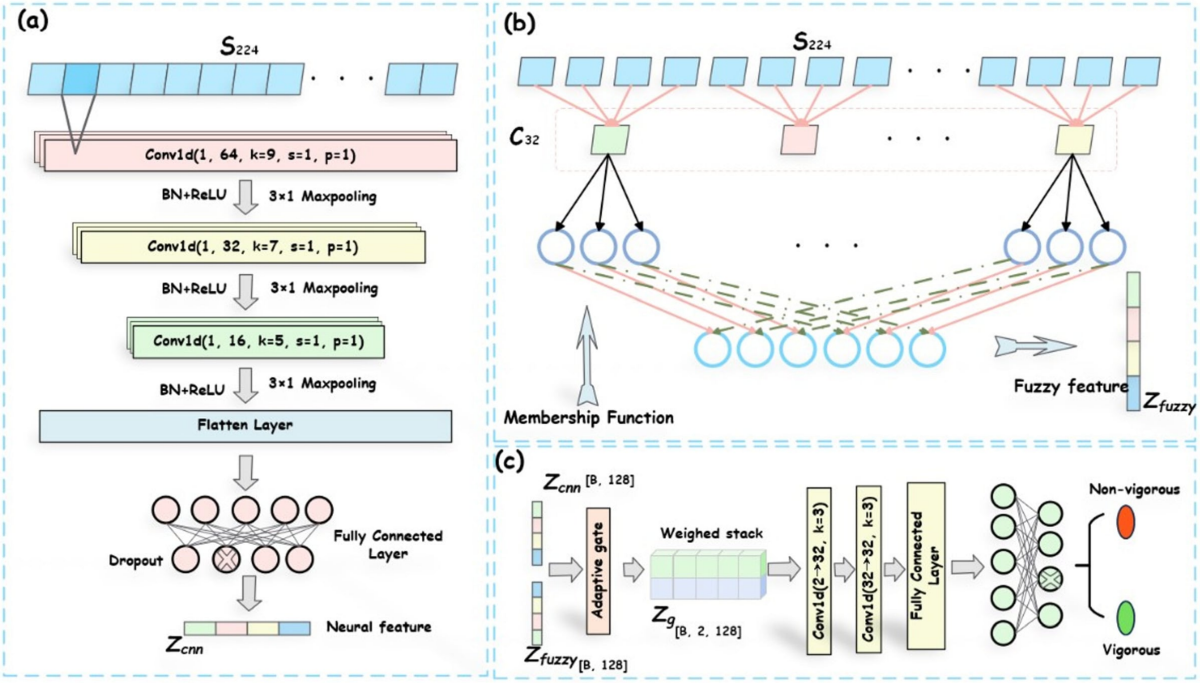


Figure 2. Model architecture of CFNet for seed vigor detection. (**a**) CNN branch, (**b**) Fuzzy branch, (**c**) Adaptive gated feature fusion.

In this branch, to enhance the model's ability to represent spectral uncertainty and continuous transitions, the 32 downsampled nodes are mapped into a fuzzy space. Specifically, for each downsampled spectral node c_j, we define M Gaussian-type membership functions:

$$f_{ij}^{s}(c_j) = e^{-\left(\frac{(c_j-\mu_{ij}^{s})^2}{(\sigma_{ij}^{s})^2}\right)}, i = 1, 2, \ldots, M \tag{5}$$

where μ_{ij}^{s} and σ_{ij}^{s} are learnable parameters denoting the center and width of the fuzzy set, respectively, and are updated via gradient descent during training. For each node c_j, its final fuzzy response is given by the product of memberships over all fuzzy sets:

$$R_j = \prod_{i=1}^{M} f_{ij}^{s}(c_j), j = 1, 2 \ldots, 32 \tag{6}$$

In effect, R_j defines the node-response set of the input layer (i.e., the downsampled sequence) in the fuzzy space. It should be emphasized that the output of this fuzzy branch is treated as a new spectral feature representation rather than a direct membership degree as in traditional fuzzy logic.

(3) Adaptive gated feature fusion

After the convolutional and fuzzy branches, two 128-dimensional feature vectors were obtained, denoted as Z_{cnn} and Z_{fuzzy}, respectively. To adaptively balance their contributions,

a branch gate was introduced before the post-convolutional fusion module. First, a branch-interaction descriptor was constructed as

$$q = \left[z_{fuzzy}, z_{cnn}, \left|z_{fuzzy} - z_{cnn}\right|, z_{fuzzy} \odot z_{cnn}\right] \tag{7}$$

where $\odot$ denotes element-wise multiplication. The descriptor was fed into a lightweight MLP followed by a softmax function to obtain two sample-wise branch weights:

$$\left[g_{fuzzy}, g_{cnn}\right] = \text{softmax}(\text{MLP}(\text{q})), g_{fuzzy} + g_{\text{cnn}} = 1 \tag{8}$$

The gated two-branch feature tensor was then defined as

$$Z_g = 2\begin{bmatrix} g_{fuzzy} z_{fuzzy} \\ g_{cnn} z_{cnn} \end{bmatrix} \tag{9}$$

where the scale factor of 2 was used to keep the feature magnitude comparable to that of the ungated two-branch representation. Z_g was subsequently processed by a post-convolutional fusion module consisting of two *Conv1d* layers, *Conv1d* $(2 \rightarrow 32, k = 3, p = 1)$ and *Conv1d* $(32 \rightarrow 32, k = 3, p = 1)$. After adaptive average pooling, dropout (0.2) and a linear classifier were used to generate the final seed vigor prediction.

During training, CFNet was optimized for 100 epochs using the Adam optimizer, with the learning rate and weight decay set to 1×10^{-3} and 1×10^{-4}, respectively. ReLU activation was used in the post-convolutional fusion module, and dropout was introduced before the classifier to alleviate overfitting. To reduce the influence of class imbalance in naturally aged rice seed samples, class-balanced focal loss was employed as the training objective instead of standard cross-entropy.

2.6.2. Comparison Model

To validate the effectiveness of the proposed fuzzy feature modeling strategy, this paper selected three representative comparative models: Partial Least Squares Discriminant Analysis (PLS-DA), Support Vector Machine (SVM), and One-Dimensional Convolutional Neural Network (1D-CNN) [27–29]. Among these, PLS-DA and SVM serve as performance baselines for traditional machine learning methods.

2.6.3. Model Evaluation Metrics

To comprehensively evaluate the model's performance in rice seed vigor classification, this study employs four metrics: *Accuracy*, *Precision*, *Recall*, and *F1-score*. The definitions of each evaluation metric are as follows:

$$Accuracy = \frac{TP + TN}{TP + TN + FP + FN} \tag{10}$$

$$Precision = \frac{TP}{TP + FP} \tag{11}$$

$$Recall = \frac{TP}{TP + FN} \tag{12}$$

$$F1 - score = \frac{2 \times Precision \times Recall}{Precision + Recall} \tag{13}$$

where TP (True Positive) refers to positive samples correctly predicted as positive, TN (True Negative) refers to negative samples correctly predicted as negative, FP (False Positive) refers to negative samples incorrectly predicted as positive, and FN (False Negative) refers to positive samples incorrectly predicted as negative.

2.7. Visualization Method

To visualize the model's attention along the spectral dimension, a gradient-weighted activation mapping mechanism was employed, defined as

$$L^{c}_{Grad-CAM++} = ReLU\left(\alpha^{c}_{k} A^{k}\right) \tag{14}$$

where A^k denotes the k-th convolutional feature map and α^c_k represents the weight coefficient computed from the gradient distribution of class c with respect to A^k. Grad-CAM++ incorporates high-order gradient terms to weight and average the gradient contributions of each band position, thereby more accurately characterizing the impact of different regions in the feature map on the output results [30]. Ultimately, the *ReLU* function is used to preserve the positive activation region, highlighting band responses that are positively correlated with the target category.

3. Results

3.1. Germination and Biochemical Analysis Results

Table 3 indicates that aging time markedly reduced the physiological performance of rice seeds. The 2024II maintained a high germination rate (>96%), whereas germination dropped sharply in the 2024I (23.14% for HH31 and 12.57% for MXZ2), suggesting a pronounced vigor decline. By the 2023II, germination was lost (0%), representing a severely aged condition. Consistently, population-level growth indices (root length and shoot length, with non-germinated seeds recorded as zero) decreased significantly with aging. As shown in Figure 3, the individual distributions shifted progressively toward lower values and became highly overlapped across stages, rather than forming clear-cut boundaries. This gradual migration and overlap at the population level highlight the soft-boundary nature of naturally aged seed vigor.

Table 3. Germination rate, growth traits, and antioxidant enzyme activities of HH31 and MXZ2 seeds at different harvest stages.

Rice Seed Variety	Indicators	2024II	2024I	2023II
HH31	Germinated rate (%)	96.57	23.14	0.00
	PRL (cm)	7.1209 ± 2.9012 ^{a}	1.0087 ± 2.3497 ^{b}	0.0000 ± 0.0000 ^{c}
	SL (cm)	4.7095 ± 1.3217 ^{a}	0.8513 ± 1.7007 ^{b}	0.0000 ± 0.0000 ^{c}
	PRW (g)	0.0102 ± 0.0075 ^{a}	0.0013 ± 0.0037 ^{b}	0.0000 ± 0.0000 ^{c}
	SW (g)	0.0171 ± 0.0065 ^{a}	0.0031 ± 0.0079 ^{b}	0.0000 ± 0.0000 ^{c}
	CAT (U/mg prot)	4.7037 ± 2.8041 ^{a}	3.3930 ± 2.4247 ^{a}	2.7707 ± 2.0467 ^{a}
	MDA (μmol/g prot)	0.6282 ± 0.2729 ^{a}	0.9905 ± 0.3367 ^{b}	1.0255 ± 0.4193 ^{b}
	SOD (U/mg prot)	1338.0675 ± 235.7507 ^{a}	1232.6890 ± 494.3535 ^{a}	1104.5201 ± 209.1248 ^{a}
MXZ2	Germinated rate (%)	98.00	12.57	0.00
	PRL (cm)	6.1587 ± 2.9636 ^{a}	0.5081 ± 1.6547 ^{b}	0.0000 ± 0.0000 ^{c}
	SL (cm)	4.5036 ± 1.2701 ^{a}	0.4546 ± 1.3419 ^{b}	0.0000 ± 0.0000 ^{c}
	PRW (g)	0.0090 ± 0.0060 ^{a}	0.0009 ± 0.0040 ^{b}	0.0000 ± 0.0000 ^{c}
	SW (g)	0.0142 ± 0.0061 ^{a}	0.0017 ± 0.0075 ^{b}	0.0000 ± 0.0000 ^{c}
	CAT (U/mg prot)	5.6453 ± 3.0034 ^{a}	5.2791 ± 4.1417 ^{a,b}	2.6031 ± 1.7119 ^{b}
	MDA (μmol/g prot)	0.6651 ± 0.3053 ^{a}	0.8490 ± 0.2685 ^{a,b}	1.0961 ± 0.4638 ^{b}
	SOD (U/mg prot)	1447.3191 ± 364.7719 ^{a}	1391.9873 ± 553.7640 ^{a}	1094.0823 ± 290.3336 ^{a}

Note: The data are presented as mean ± standard deviation. According to the results of the post-hoc test, different letters in the same row indicate a statistically significant difference between time points ($p < 0.05$). CAT activity (U·mg^{-1} protein), MDA content (μmol·g^{-1} protein), SOD activity (U·mg^{-1} protein).

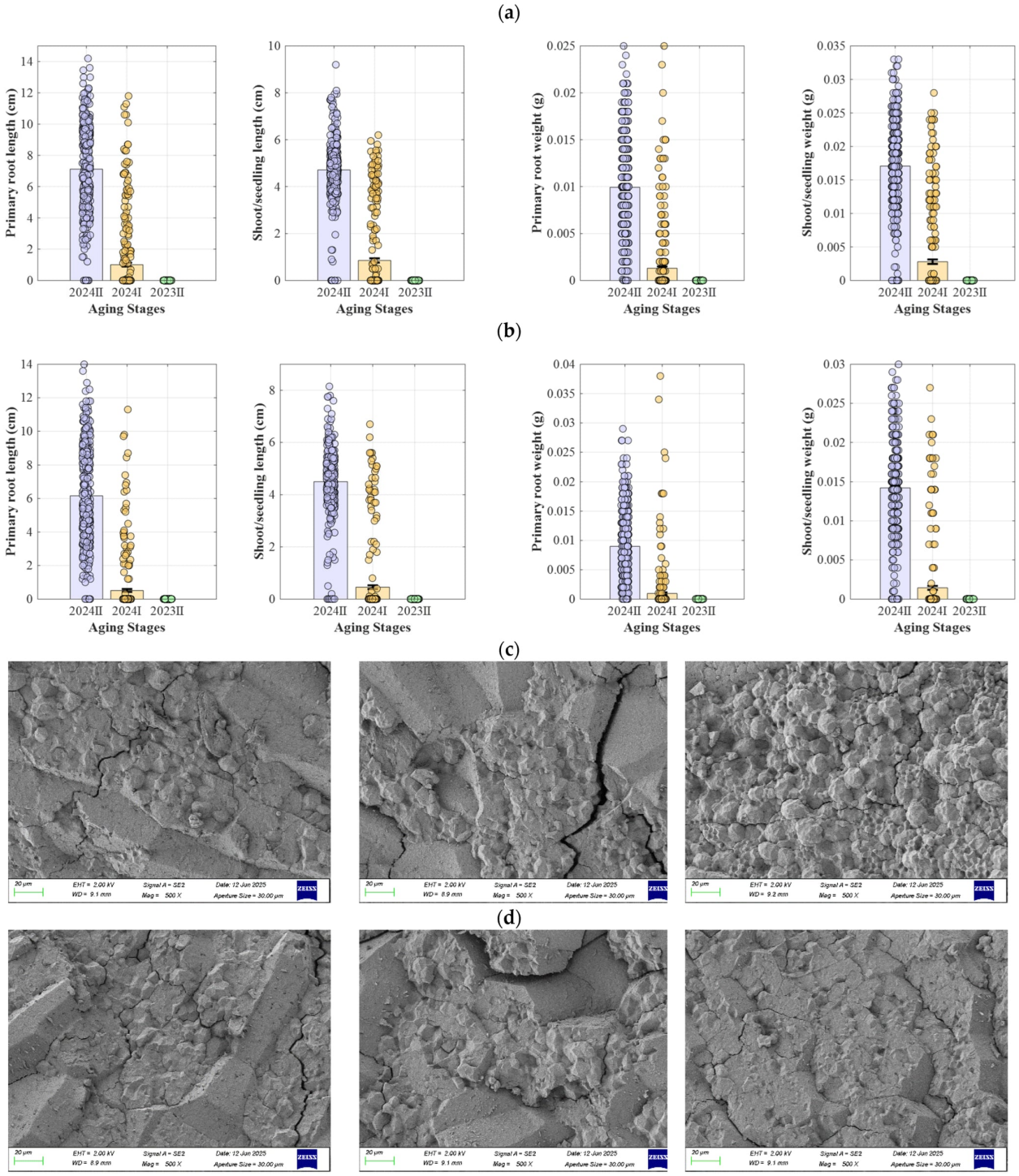


Figure 3. Scatter plots of physiological traits of rice seeds from two cultivars (HH31 and MXZ2) harvested at three stages. (**a**,**b**) Root and shoot traits (length and weight) of HH31 and MXZ2. (**c**,**d**) Starch granule micrographs of HH31 and MXZ2 under natural aging, from left to right, images correspond to 2024II, 2024I, and 2023II, respectively.

Based on the criteria in Section 2.3, the SVI was subsequently calculated. The results indicated that HH31 contained 392 high-vigor seeds and 658 low-vigor or non-vigorous seeds, while MXZ2 comprised 370 high-vigor seeds and 680 low-vigor or non-vigorous seeds.

As shown in Table 3, antioxidant-related indicators exhibited consistent aging-dependent trends across both rice varieties. With increasing storage duration, CAT and SOD activities showed an overall declining tendency, whereas MDA content increased

progressively. These changes indicate that seed antioxidant status is altered during natural aging, with enhanced lipid peroxidation accompanying prolonged storage [31].

Specifically, CAT activity showed a numerical decline with seed aging, decreasing from 4.7037 ± 2.8041 to 2.7707 ± 2.0467 U mg^{-1} protein in HH31 and from 5.6453 ± 3.0034 to 2.6031 ± 1.7119 U mg^{-1} protein in MXZ2. The differences among the three stages were not significant for HH31. In MXZ2, CAT activity was significantly lower in 2023II than in 2024II, whereas the 2024I group did not differ significantly from either stage. SOD activity showed a similar numerical trend, but the differences among stages were not significant in either cultivar. This lack of a significant difference is consistent with the findings of Yin et al. [32] for SOD activity in artificially aged rice seeds. MDA showed an overall increasing tendency during aging. In HH31, MDA levels were higher in 2024I and 2023II than in 2024II, while the difference between 2024I and 2023II was not significant. In MXZ2, MDA was significantly higher in 2023II than in 2024II, whereas the 2024I group showed an intermediate level and did not differ significantly from either stage.

Additionally, seed senescence is a complex physiological degradation process influenced not only by ROS levels and antioxidant system regulation but also by the dynamic changes in stored substances. The endosperm, as the primary nutrient source during early seed germination, also affects the senescence process [15]. As shown in Figure 3, as seed aging time increases, the starch stored in the endosperm gradually breaks down, and its structure shifts from being regular and dense to loose and fragmented. Visible small pores appear between starch granules, indicating that their integrity has been compromised, which may further limit the energy supply needed for germination.

3.2. Spectral Analysis

Figure 4 presents the mean spectral curves of HH31 and MXZ2 seeds at different vigor levels. While the spectral profiles of the two cultivars shared similar shapes, distinct reflectance differences were observed at specific wavelengths.

In the VNIR region, key absorption features were observed at approximately 420–550 nm and around 700 nm, mainly associated with surface pigments [33]. As seeds age, the degradation and oxidation of these pigments lead to increased reflectance, particularly in low-vigor samples. The region near 750–800 nm mainly reflects weak C–H and O–H combination absorptions [34], while the feature around 930 nm corresponds to O–H combination bands linked to cellular moisture status [35]. The progressive attenuation of these signals across aging stages indicates pigment loss, membrane degradation, and reduced physiological water, all of which contribute to the decline in seed vigor.

In the SWIR range, distinct absorption bands appeared at 970, 1200, 1450, and 1680 nm; 970 nm is linked to the overtone absorption of O–H, 1200 nm corresponds to the second overtone of C–H bonds [36], whereas the strong feature at 1450 nm reflects the first overtone of O–H stretching from tightly bound water superimposed by a weak N–H first-overtone component of amide A near 1550 nm [37], and the band around 1680 nm is predominantly associated with the first overtone of C–H stretching in lipids, reflecting lipid degradation during seed aging [38]. Overall, non-vigorous seeds exhibited higher reflectance than vigorous seeds over much of the SWIR range, indicating reduced water content and increased degradation of starch and lipids, which aligns with the results in spectral analysis. Near the long-wavelength end of the SWIR range, this pattern reversed, with non-vigorous seeds exhibiting lower reflectance than vigorous seeds, likely due to lipid peroxidation and accumulated protein oxidative modifications during storage (evidenced by increased MDA levels). These findings align with biochemical analyses and confirm that spectral features can effectively characterize physiological changes during seed aging, including water loss and membrane lipid oxidation.

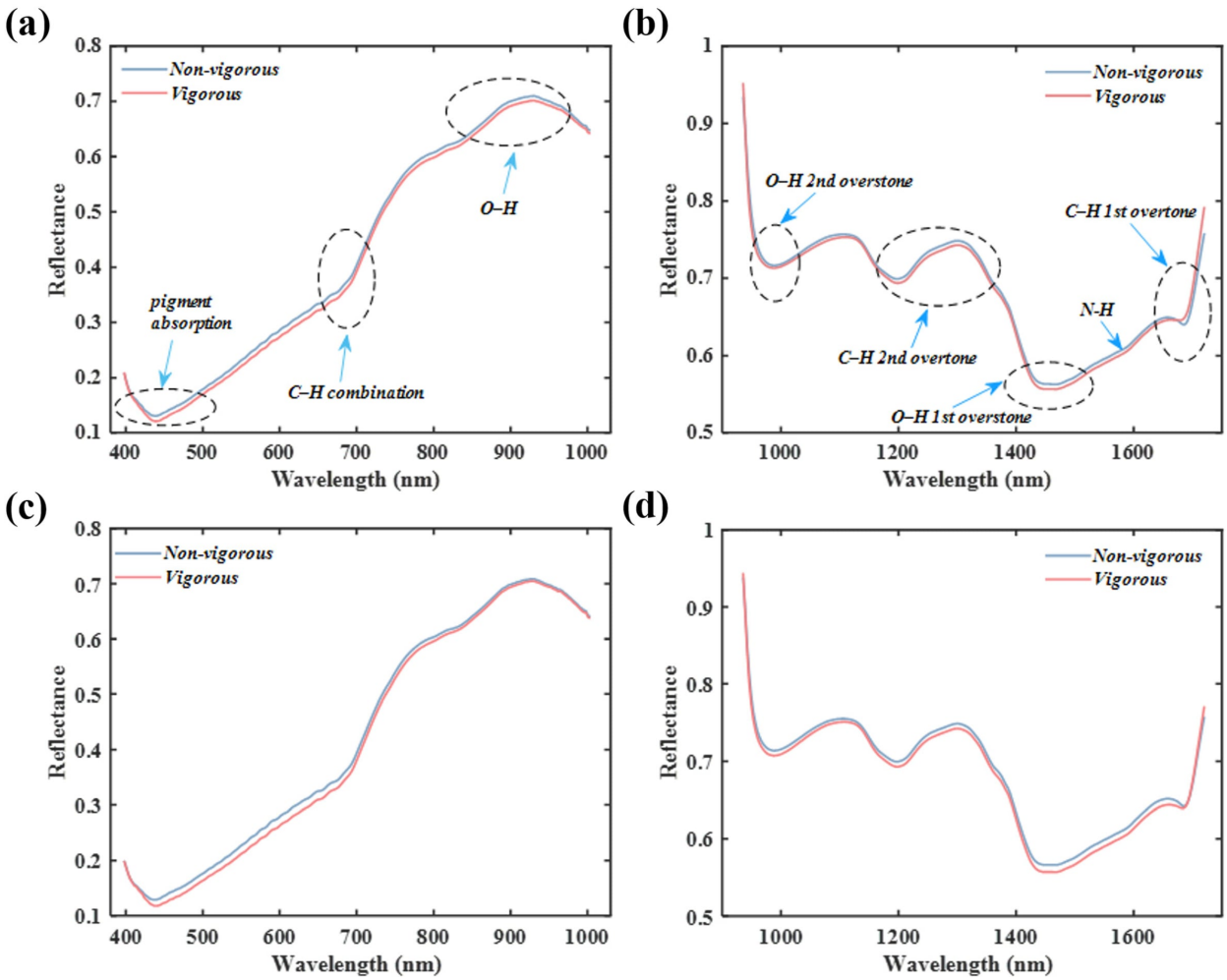


Figure 4. Average spectral curves of seeds with different vigor, (**a**) HH31-VNIR, (**b**) HH31-SWIR, (**c**) MXZ2-VNIR, (**d**) MXZ2-SWIR.

3.3. Model Performance

Tables 4 and S1 show that the classification performance of rice seed vigor varied substantially depending on the rice variety, spectral range, and modeling strategy. In general, CFNet achieved the highest test accuracy and F1-score among the evaluated models across all four variety–spectral range combinations.

Table 4. Classification performance of different models for two rice varieties (HH31 and MXZ2) across VNIR and SWIR spectral ranges.

Variety	Spectral Range	Model	Train (%)	Val (%)	Test (%)			
			Accuracy	Accuracy	Accuracy	Precision	Recall	F1-Score
HH31	VNIR	PLS-DA	62.06	66.67	63.81	64.84	65.72	63.54
		SVM	50.95	60.48	61.43	69.82	67.58	61.17
		CNN	85.56	68.10	70.48	71.85	73.07	70.30
		CFNet	85.08	76.19	79.52	78.73	76.80	77.50
	SWIR	PLS-DA	78.10	72.86	77.62	76.39	77.54	76.73
		SVM	80.95	77.62	76.19	76.44	78.15	75.88
		CNN	91.27	84.29	85.71	85.04	84.28	84.62
		CFNet	93.97	85.24	90.95	90.63	89.98	90.29

Table 4. *Cont.*

Variety	Spectral Range	Model	Train (%)	Val (%)	Test (%)			
			Accuracy	Accuracy	Accuracy	Precision	Recall	F1-Score
MXZ2	VNIR	PLS-DA	82.54	81.43	82.38	82.79	77.77	79.30
		SVM	98.25	83.81	83.33	81.67	83.44	82.29
		CNN	88.25	84.29	80.48	79.34	81.85	79.70
		CFNet	91.90	85.71	87.14	85.85	86.07	85.96
	SWIR	PLS-DA	71.43	68.57	65.71	60.66	57.20	56.66
		SVM	81.75	68.57	69.05	68.03	69.63	67.94
		CNN	78.73	71.90	73.33	70.92	71.40	71.13
		CFNet	80.63	73.33	73.81	71.47	72.08	71.73

3.3.1. Model Performance for HH31

The classification performance of HH31 varied markedly between VNIR and SWIR (Table 4 and Figure S1a,b). In the VNIR range, PLS-DA and SVM showed limited classification ability, with test accuracies of 63.81% and 61.43%, respectively. Their confusion matrices showed considerable misclassification between non-vigorous and vigorous seeds, indicating that the VNIR spectra of HH31 were weakly separable using conventional classifiers. CNN improved the test accuracy to 70.48% and the F1-score to 70.30%, suggesting that nonlinear convolutional feature extraction captured more useful spectral information than traditional models. CFNet achieved the best VNIR performance, with a test accuracy of 79.52%, Precision of 78.73%, Recall of 76.80%, and F1-score of 77.50%. Compared with CNN, CFNet improved test accuracy by 9.04 percentage points and F1-score by 7.20%. CFNet reduced the total number of misclassified seeds from 62 with CNN to 43, mainly because fewer low-vigor or non-vigorous seeds were classified as high vigor (Figure S1a).

In the SWIR range, all models performed better than in VNIR, indicating that SWIR provided more discriminative information for HH31 vigor classification. PLS-DA and SVM achieved test accuracies of 77.62% and 76.19%, respectively, while CNN increased the test accuracy to 85.71%. CFNet obtained the highest performance, with a test accuracy of 90.95%, Precision of 90.63%, Recall of 89.98%, and F1-score of 90.29%. The confusion matrices in Figure S1a,b showed fewer classification errors in SWIR than in VNIR, and CFNet produced the most balanced class-level prediction among the compared models. These results indicate that HH31 seed vigor was more effectively discriminated in the SWIR range than in the VNIR range.

3.3.2. Model Performance for MXZ2

For MXZ2, the optimal spectral range differed from HH31 (Table 4 and Figure S1c,d). In the VNIR range, PLS-DA and SVM achieved relatively high test accuracies of 82.38% and 83.33%, respectively, suggesting that VNIR spectra contained useful vigor-related information for MXZ2. However, their class-level prediction patterns were not equally balanced. For example, PLS-DA correctly identified most non-vigorous seeds but missed more vigorous seeds, which was reflected by its lower Recall and F1-score. CNN achieved a test accuracy of 80.48% and an F1-score of 79.70%. CFNet further improved the test accuracy to 87.14%, with Precision, Recall, and F1-score reaching 85.85%, 86.07%, and 85.96%, respectively. The gain in test accuracy mainly reflected a reduction in the number of low-vigor or non-vigorous seeds misclassified as high vigor (Figure S1c).

In the SWIR range, the overall classification performance of MXZ2 was lower than that in VNIR. PLS-DA showed weak discrimination, with a test accuracy of 65.71% and an F1-score of only 56.66%. Its confusion matrix indicated a clear bias toward non-vigorous predictions, with many vigorous seeds being misclassified. SVM and CNN alleviated this issue to some extent, achieving test accuracies of 69.05% and 73.33%, respectively. CFNet

achieved the best result in this condition, with a test accuracy of 73.81% and an F1-score of 71.73%. However, the improvement over CNN was relatively small, indicating that the SWIR spectra of MXZ2 were less discriminative for vigor classification than the VNIR spectra.

3.4. Ablation Experiment

To evaluate the contribution of the convolutional branch, fuzzy branch, and adaptive gate, ablation experiments were performed on HH31-SWIR and MXZ2-VNIR, which were the optimal spectral ranges for the two varieties. Four variants were compared: (A) CNN-only, identical to the 1D-CNN baseline in Table 4; (B) Fuzzy-only; (C) CNN + Fuzzy without gate, using fixed equal branch weights; and (D) CFNet, using adaptive branch weighting before fusion convolution.

The ablation results in Table 5 further clarify the role of each CFNet component. The performance of the fuzzy-only branch depended on the cultivar and spectral range. It was lower than the CNN-only model for HH31-SWIR but higher than the CNN-only model for MXZ2-VNIR, indicating that the standalone contribution of fuzzy features was dependent on the cultivar and spectral range rather than uniformly inferior to CNN features. This behavior was consistent with the t-SNE visualization in Figure 5, where the Fuzzy-only features exhibited strong overlap between vigorous and non-vigorous samples. Therefore, the fuzzy branch should not be interpreted as an independent classifier. However, when the fuzzy branch was combined with the CNN branch, the feature distribution became more separable and the classification performance improved. This suggests that the fuzzy branch provided complementary soft-boundary information rather than standalone discriminative features. In particular, CNN features captured the main local spectral patterns, while fuzzy features described the continuous responses of downsampled spectral nodes. Their combination helped refine the fused feature representation under naturally aged conditions.

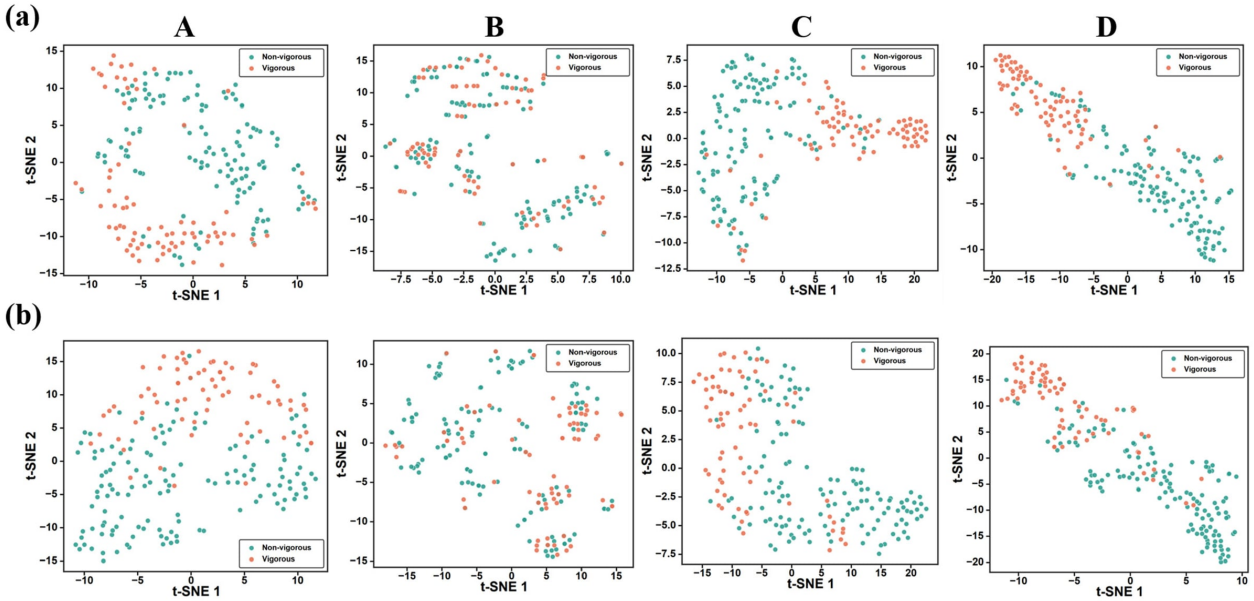


Figure 5. t-SNE visualization of ablation variants under the optimal spectral ranges of two rice cultivars. (**A**) CNN-only, (**B**) Fuzzy-only, (**C**) CNN + Fuzzy without gate, (**D**) CFNet. (**a**) HH31@SWIR; (**b**) MXZ2@VNIR.

After introducing the adaptive branch gate, CFNet produced the most organized feature distribution in the t-SNE space, with clearer class-dominant regions than the ungated two-branch model. This indicates that sample-specific branch weighting helped regulate the contribution of CNN and fuzzy features before fusion convolution. Overall, the ablation

and t-SNE results suggest that the effectiveness of CFNet arises from the complementary interaction between convolutional features and fuzzy representations, rather than from the fuzzy branch alone.

Table 5. Ablation study of CFNet components under the optimal spectral ranges of two rice varieties.

Variety	Range	Variant	CNN	Fuzzy	Adaptive Gate	Train	Val	Test	
						Acc (%)	Acc (%)	Acc (%)	F1-Score (%)
HH31	SWIR	A	✓	×	×	91.27	84.29	85.71	84.62
		B	×	✓	×	83.49	77.62	82.86	81.44
		C	✓	✓	×	91.43	88.10	87.62	86.81
		D	✓	✓	✓	93.97	85.24	90.95	90.29
MXZ2	VNIR	A	✓	×	×	88.25	84.29	80.48	79.70
		B	×	✓	×	93.33	84.76	86.19	85.25
		C	✓	✓	×	89.68	88.10	86.67	84.89
		D	✓	✓	✓	91.90	85.71	87.14	85.96

3.5. Visualization of the Model

Figure 6 presents the Grad-CAM++ visualization results of CNN and CFNet for HH31 and MXZ2. For HH31, CFNet showed stronger activation for high-vigor seeds near 1200 nm and across much of the 1400–1500 nm range. Around 1400–1500 nm, the two class activation curves were farther apart for CFNet than for CNN. Low-vigor or non-vigorous seeds showed stronger activation near 1070 and 1660 nm in the CFNet profiles. The CAT, SOD, and MDA measurements in Table 3 provide biochemical context for seed aging. However, whether the highlighted wavelengths are related to the measured biochemical changes remains to be verified.

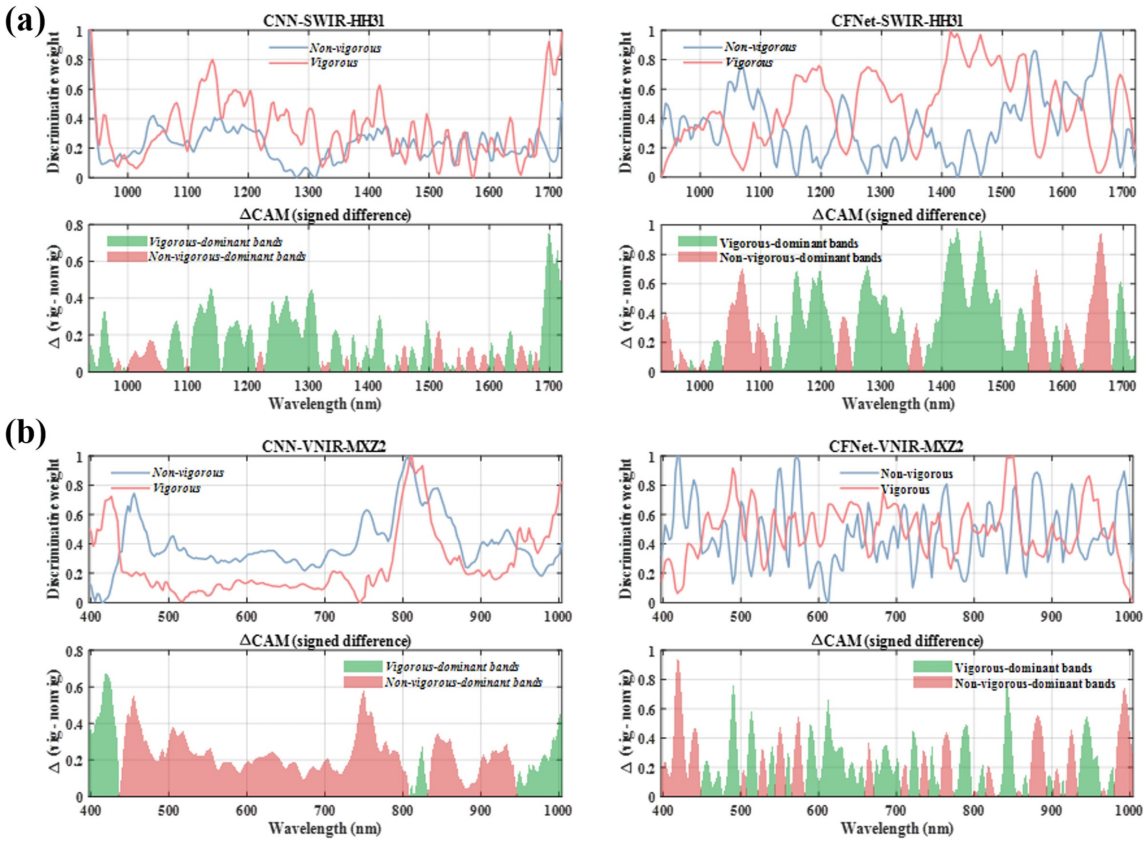


Figure 6. One-dimensional Grad-CAM++ visualization of the CFNet model under the optimal spectral range (top: class-wise curves, bottom: inter-class difference), (**a**) HH31-SWIR, (**b**) MXZ2-VNIR.

For MXZ2, CNN showed stronger activation for low-vigor or non-vigorous seeds over much of the 450–780 nm range. In the CFNet profiles, the differences between classes were concentrated in narrower wavelength intervals. For example, activation was stronger for high-vigor seeds near 490 and 850 nm and for low-vigor or non-vigorous seeds near 420 and 880 nm. Overall, compared with CNN, CFNet showed greater contrast between the two vigor classes at selected wavelengths in the Grad-CAM++ profiles.

3.6. GUI-Based Rice Seed Vigor Assessment Platform

A Python-based graphical user interface (GUI) was developed to demonstrate the workflow of non-destructive rice seed vigor assessment using previously acquired hyperspectral images. As shown in Figure 7, users can load a hyperspectral TIFF image and obtain individual-seed predictions and summary statistics. The input image and classification map are displayed side by side. Green contours indicate seeds predicted as high vigor, whereas red contours indicate seeds predicted as low vigor or non-vigorous. The statistical panel reports the number of seeds in each class and the predicted high-vigor fraction.

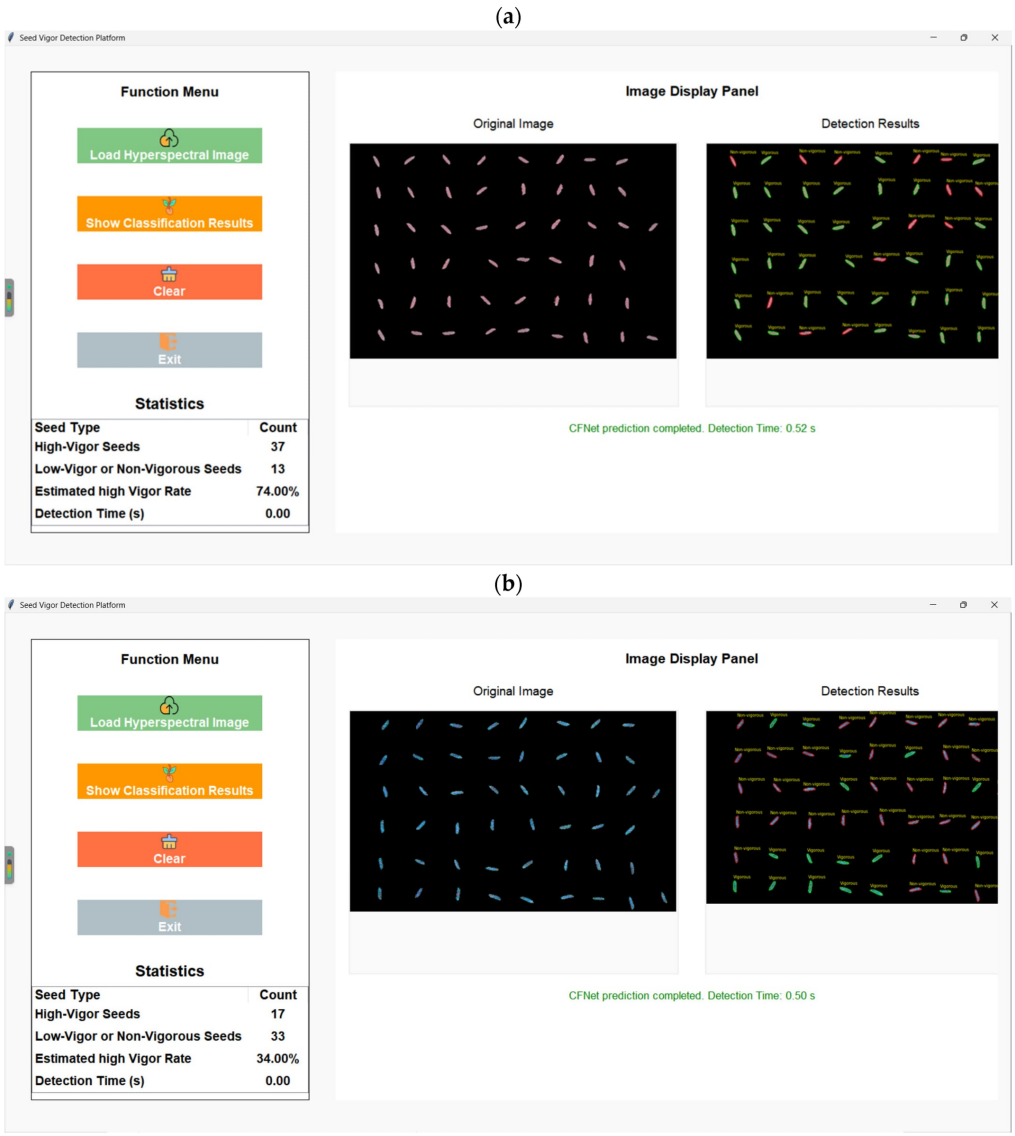


Figure 7. Rice seed vigor assessment platform. (**a**) Detection results for HH31; (**b**) detection results for MXZ2. Note: Green contours indicate vigorous seeds, while red contours represent non-vigorous seeds.

Seed regions were identified using Otsu thresholding and contour extraction. Spectra extracted from individual-seed regions were standardized using the saved training-stage scaler and passed to the pretrained classifier. The GUI was run on a Windows 11 computer equipped with an AMD Ryzen 7 5800H processor, approximately 32 GB RAM, and an NVIDIA GeForce RTX 3060 Laptop GPU. The software used CUDA.

In single-run measurements, the processing time per hyperspectral image was approximately 0.52 s for HH31 and 0.50 s for MXZ2. Timing started when classification was initiated after image loading and initial seed segmentation. The timed interval included spectral extraction, standardization, prediction, result plotting and saving, and updates to the GUI widgets. The GUI could support laboratory seed-lot assessment by allowing users to inspect individual-seed predictions and summarize the predicted high-vigor fraction of an imaged sample.

4. Discussion

Hyperspectral imaging has been widely used for non-destructive seed viability and vigor assessment, and previous studies have reported promising results in corn, rice, and maize seeds [11,15,36,39]. However, a key difference between many previous studies and the present work lies in the deterioration scenario. Artificial aging, heat damage, frost damage, or storage-year discrimination often generates relatively discrete physiological states, making spectral differences easier to capture using conventional chemometric or deep learning models [16,26,31,38]. In contrast, naturally aged seeds under real storage conditions undergo gradual and heterogeneous deterioration. Therefore, the analytical target in this study was not a sharply separated viability state, but a weakly separable vigor status derived from germination and early seedling growth. This difference explains why naturally aged rice seed vigor discrimination remains more challenging than controlled viability classification [40].

The physiological and biochemical results further support this interpretation. Although germination-related traits decreased markedly with storage time, some biochemical indicators, such as CAT and SOD, showed only decreasing tendencies without significant differences among all aging stages. This does not indicate that aging-related changes were absent; rather, it suggests that antioxidant deterioration under natural aging was gradual and heterogeneous. Meanwhile, the increase in MDA content indicated the accumulation of lipid peroxidation, which is consistent with oxidative damage during seed aging [19,32]. The year-wise spectral distributions in Figure S2 further support this interpretation. Unlike artificial aging, which often produces more discrete deterioration states, natural aging generated gradual spectral transitions among harvest-year groups. In particular, the 2024I group contained many intermediate seeds with partially retained vigor, resulting in substantial spectral overlap with both the fresher 2024II group and the severely aged 2023II group. This weak spectral separability indicates that sharp decision boundaries are intrinsically difficult to establish under natural aging, even when nonlinear classifiers are used.

Under this condition, CFNet showed advantages over PLS-DA, SVM, and CNN, but the ablation results indicate that the improvement should not be attributed to the fuzzy branch as an independent classifier. The Fuzzy-only variant showed condition-dependent discrimination and substantial feature overlap in some conditions, showing that fuzzy features alone did not provide a consistently reliable separation across the two experimental conditions. However, when fuzzy features were fused with CNN features, both classification performance and feature separability improved. This suggests that the fuzzy branch provided complementary information to the convolutional branch, most likely by describing continuous responses of downsampled spectral nodes rather than extracting strong standalone discriminative features. This role is consistent with the general use of

fuzzy modeling for representing uncertainty and ambiguous boundaries [23–25], but in this study the ambiguity originates from biological continuity during natural seed aging rather than only from external noise or spectral fluctuation.

The Grad-CAM++ results provide a further explanation of how CFNet improved the spectral representation. Compared with CNN, CFNet produced more distinct class-discriminative responses in the optimal spectral ranges, indicating that the fused representation enhanced differences between vigorous and non-vigorous seeds in biologically relevant spectral regions. For HH31, the important SWIR regions were associated with water status, C-H/O-H-related absorptions, lipid degradation, and protein-related changes, while for MXZ2 the VNIR responses were more related to pigment- and moisture-sensitive regions. These patterns are consistent with the physiological deterioration observed during natural aging and with previous reports that seed aging affects moisture, membrane integrity, reserve substances, and oxidative status. Therefore, CFNet improved not only the numerical classification results but also the traceability of spectral decision-making.

Another important observation is the cultivar-dependent spectral sensitivity. HH31 achieved its best performance in SWIR, whereas MXZ2 performed best in VNIR. This suggests that the optimal spectral range for vigor assessment may depend on cultivar-specific seed composition, surface characteristics, and aging response. Similar material-dependent spectral behavior has been reported in hyperspectral studies of agricultural and food products, where the effectiveness of spectral regions varied with sample type, chemical composition, and target attribute [34]. Therefore, a universal wavelength range or model setting may not be sufficient for practical seed vigor screening across cultivars. Although the online platform demonstrated the feasibility of rapid seed-level detection, broader validation using more cultivars, harvest years, storage environments, and independent external datasets is still necessary before large-scale deployment.

5. Conclusions

This study developed a CFNet for hyperspectral identification of naturally aged rice seed vigor. By combining convolutional feature extraction with fuzzy membership-based representation and adaptive branch weighting, CFNet was designed to accommodate the weakly separable spectral characteristics caused by gradual vigor deterioration. Across two rice varieties and two spectral ranges, CFNet achieved the best performance among the evaluated models. The optimal spectral range was cultivar-dependent, with HH31 performing best in SWIR and MXZ2 in VNIR. Under these optimal conditions, CFNet achieved 90.95% accuracy and 90.29% F1-score for HH31-SWIR, and 87.14% accuracy and 85.96% F1-score for MXZ2-VNIR. Ablation and feature visualization analyses indicated that the fuzzy branch alone was not sufficient for direct classification, but it contributed complementary information when fused with CNN features. Grad-CAM++ further showed that CFNet enhanced class-discriminative spectral responses, supporting the interpretability of the proposed model. These findings suggest that soft-boundary feature modeling is a feasible strategy for improving hyperspectral vigor assessment of naturally aged seeds. Further work should evaluate the generalization of CFNet across broader cultivar groups, storage conditions, and independent external datasets, and examine its transferability to other seed quality assessment tasks.

Supplementary Materials: The following supporting information can be downloaded at https://www.mdpi.com/article/10.3390/agriculture16232631/s1: Figure S1: Confusion matrices of different models for vigor classification in naturally aged rice seeds. (a) HH31@VNIR, (b) HH31@SWIR, (c) MXZ2@VNIR, (d) MXZ2@SWIR; Figure S2: Mean spectral curves of three natural aging stages (2024II, 2024I, 2023II) in rice seeds. (a), HH31; (b), MXZ2; Table S1: Performance comparison of

traditional and deep learning models for vigor classification in naturally aged rice seeds (Precision, Recall, F1-score).

Author Contributions: S.T.: Writing—original draft, investigation, software; Y.Z.: writing—review & editing, supervision; J.Y.: data curation; Z.C.: data curation; Z.Q.: data curation; H.W.: software; L.Q.: investigation, funding acquisition; N.Z.: investigation, supervision; X.F.: investigation, funding acquisition. All authors have read and agreed to the published version of the manuscript.

Funding: Guangdong S&T Program (2023B0202130001), Guangdong Special Support Program—Provincial Department of Agriculture and Rural Affairs (Agriculture and Rural Vitalization Talent) [NYLJ2024004], specific university discipline construction project (2023B10564002).

Data Availability Statement: The data supporting the findings of this study are available from the corresponding authors upon reasonable request.

Acknowledgments: During the preparation of this manuscript, the authors used ChatGPT (OpenAI, GPT-5.6) for language polishing and grammatical refinement. The authors reviewed and edited the AI-assisted content and take full responsibility for the final manuscript.

Conflicts of Interest: The authors declare no conflict of interest.

References

1. Ge, Y.; Song, S.; Yu, S.; Zhang, X.; Li, X. Rice Seed Classification by Hyperspectral Imaging System: A Real-World Dataset and a Credible Algorithm. *Comput. Electron. Agric.* **2024**, *219*, 108776. [CrossRef]
2. Dehbasteh, M.; Naderi Tehrani, N.; Parastar, H. Multivariate Curve Resolution Followed by Partial Least Squares-Discriminant Analysis Combined with Vis-NIR Hyperspectral Imaging for Riceauthentication. *Food Res. Int.* **2025**, *221*, 117266. [CrossRef] [PubMed]
3. Zhou, Y.; Feng, X.; Tang, S.; Yang, J.; Chen, S.; Meng, X.; Liang, Z.; Ma, R.; Qi, L. Dual Attention Guided Context-Aware Feature Learning for Residual Unfilled Grains Detection on Threshed Rice Panicles. *Artif. Intell. Agric.* **2026**, *16*, 514–528. [CrossRef]
4. Li, H.; Mao, Y.; Xu, Y.; Tu, K.; Zhang, H.; Gu, R.; Sun, Q. Rapid Detection of the Viability of Naturally Aged Maize Seeds Using Multimodal Data Fusion and Explainable Deep Learning Techniques. *Food Chem.* **2025**, *478*, 143692. [CrossRef] [PubMed]
5. Šrámková, P.; Švubová, R.; Kostoláni, D.; Kyzek, S.; Bathoova, M.; Gálová, E.; Ďurčányová, S.; Stupavská, M.; Kováčik, D.; Zahoranová, A. Effect of Cold Atmospheric Pressure Plasma Treatment on Germination, Growth, and Surface Properties of Pea Seeds: A Scalability and Energy Efficiency Analysis of DCSBD Plasma Systems. *Innov. Food Sci. Emerg. Technol.* **2026**, *107*, 35001. [CrossRef]
6. Cheng, T.; Chen, G.; Wang, Z.; Hu, R.; She, B.; Pan, Z.; Zhou, X.G.; Zhang, G.; Zhang, D. Hyperspectral and Imagery Integrated Analysis for Vegetable Seed Vigor Detection. *Infrared Phys. Technol.* **2023**, *131*, 104605. [CrossRef]
7. Bernardo Oliveira, D.G.D.; Gorla, G.; de Medeiros, E.P.; Simões, S.d.S.; Amigo, J.M.; Pimentel, M.F. Cottonseed Germination Prediction with Non-Destructive NIR Strategies. *Talanta* **2026**, *298*, 129017. [CrossRef]
8. Li, Q.; Zhao, J.; Tu, K.; Liu, J.; Lan, W.; Pan, L. Enhanced Classification of Unsound Sorghum Kernels Based on Decision-Level Fusion of Hyperspectral and Imaging Textural Features. *Innov. Food Sci. Emerg. Technol.* **2026**, *107*, 104373. [CrossRef]
9. Li, J.C.; Song, J.Y.; Bian, Z.S.Q.L.F.; Yang, C. Multi-Laser Hyperspectral Imaging System for Food Quality Assessment. *Innov. Food Sci. Emerg. Technol.* **2026**, *107*, 104368. [CrossRef]
10. Tang, S.; Zhang, L.; Tian, X.; Zheng, M.; Zhang, H.; Zhong, N. Synergizing Meat Science and Interpretable AI: Quantifying Crispness Gradients for Quality Authentication of Tilapia Fillet Processing. *Food Chem.* **2025**, *484*, 144252. [CrossRef] [PubMed]
11. Ma, T.; Tsuchikawa, S.; Inagaki, T. Rapid and Non-Destructive Seed Viability Prediction Using near-Infrared Hyperspectral Imaging Coupled with a Deep Learning Approach. *Comput. Electron. Agric.* **2020**, *177*, 105683. [CrossRef]
12. Tang, S.; Zhong, N.; Zhou, Y.; Chen, S.; Dong, Z.; Qi, L.; Feng, X. Synergistic Spectral-Spatial Fusion in Hyperspectral Imaging: Dual Attention-Based Rice Seed Varieties Identification. *Food Control* **2025**, *176*, 111411. [CrossRef]
13. Wu, N.; Weng, S.; Xiao, Q.; Jiang, H.; Zhao, Y.; He, Y. Rapid and Accurate Identification of Bakanae Pathogens Carried by Rice Seeds Based on Hyperspectral Imaging and Deep Transfer Learning. *Spectrochim. Acta A Mol. Biomol. Spectrosc.* **2024**, *311*, 123889. [CrossRef] [PubMed]
14. Mensah, B.; Prasifka, J.; Hulke, B.; Monono, E.; Sun, X. Detection of Insect-Damaged Sunflower Seeds Using near-Infrared Hyperspectral Imaging and Machine Learning. *Smart Agric. Technol.* **2025**, *12*, 101110. [CrossRef]
15. Wu, N.; Weng, S.; Chen, J.; Xiao, Q.; Zhang, C.; He, Y. Deep Convolution Neural Network with Weighted Loss to Detect Rice Seeds Vigor Based on Hyperspectral Imaging under the Sample-Imbalanced Condition. *Comput. Electron. Agric.* **2022**, *196*, 106850. [CrossRef]

16. Zhang, L.; Rao, Z.; Ji, H. Hyperspectral Imaging Technology Combined with Multivariate Data Analysis to Identify Heat-Damaged Rice Seeds. *Spectrosc. Lett.* **2020**, *53*, 207–221. [CrossRef]
17. He, X.; Feng, X.; Sun, D.; Liu, F.; Bao, Y.; He, Y. Rapid and Nondestructive Measurement of Rice Seed Vitality of Different Years Using Near-Infrared Hyperspectral Imaging. *Molecules* **2019**, *24*, 2227. [CrossRef] [PubMed]
18. Jin, B.; Qi, H.; Jia, L.; Tang, Q.; Gao, L.; Li, Z.; Zhao, G. Determination of Viability and Vigor of Naturally-Aged Rice Seeds Using Hyperspectral Imaging with Machine Learning. *Infrared Phys. Technol.* **2022**, *122*, 104097. [CrossRef]
19. An, T.; Fan, Y.; Tian, X.; Wang, Q.; Wang, Z.; Fan, S.; Huang, W. Green Analytical Assay for the Viability Assessment of Single Maize Seeds Using Double-Threshold Strategy for Catalase Activity and Malondialdehyde Content. *Food Chem.* **2024**, *455*, 139889. [CrossRef] [PubMed]
20. Xia, Y.; Xu, Y.; Li, J.; Zhang, C.; Fan, S. Recent Advances in Emerging Techniques for Non-Destructive Detection of Seed Viability: A Review. *Artif. Intell. Agric.* **2019**, *1*, 35–47. [CrossRef]
21. Ding, W.; Lin, J.; Li, C.; Zhu, Z.; Wu, C.; Cao, J.; Liu, D.; Zhang, Y.; Yang, Q.; Xing, A.; et al. Development of a Comprehensive Evaluation System and Models to Determine Soybean Seed Vigor. *Ind. Crops Prod.* **2025**, *224*, 120329. [CrossRef]
22. Zhao, N.; Duan, Z.; Li, Q.; Guo, K.; Zhang, Z.; Liu, B. A Cable Insulation Defect Classification Method Based on CNN-Transformer. *Front. Phys.* **2024**, *12*, 1432527. Correction in *Front. Phys.* **2025**, *13*, 1653145. [CrossRef]
23. Li, D.; Xu, Z.; Lin, R.; Huang, Y.; Ouyang, Q.; Liu, Z. SIFNet: A Spectrum-Image Fusion Neural Network in Hyperspectral Imaging for Intelligent Quality Assessment of Crude Tea to Ensure Tea Product Availability. *Comput. Electron. Agric.* **2026**, *243*, 111441. [CrossRef]
24. Gong, A.; Huang, W.; Xiao, Y.; Yu, Y.; Guo, L. CFNet: Cross-Modal Data Augmentation Empowered Fuzzy Neural Network for Spectral Fluctuation. *Knowl. Based Syst.* **2024**, *304*, 112450. [CrossRef]
25. Serrano-Guerrero, J.; Romero, F.P.; Olivas, J.A. Fuzzy Logic Applied to Opinion Mining: A Review. *Knowl. Based Syst.* **2021**, *222*, 107018. [CrossRef]
26. Zhu, H.; Yang, R.; Lu, M.; Shi, W.; Sun, W.; Lv, D.; Liu, H.; Wu, Q.; Jiang, X.; Han, Z. Identification of Maize Seed Vigor under Different Accelerated Aging Times Using Hyperspectral Imaging and Spectral Deep Features. *Comput. Electron. Agric.* **2025**, *231*, 109980. [CrossRef]
27. Sampaio, P.S.; Castanho, A.; Almeida, A.S.; Oliveira, J.; Brites, C. Identification of Rice Flour Types with Near-Infrared Spectroscopy Associated with PLS-DA and SVM Methods. *Eur. Food Res. Technol.* **2020**, *246*, 527–537. [CrossRef]
28. Chunhui, Z.; Bing, G.; Lejun, Z.; Xiaoqing, W. Classification of Hyperspectral Imagery Based on Spectral Gradient, SVM and Spatial Random Forest. *Infrared Phys. Technol.* **2018**, *95*, 61–69. [CrossRef]
29. Han, D.; Liu, Q.; Fan, W. A New Image Classification Method Using CNN Transfer Learning and Web Data Augmentation. *Expert Syst. Appl.* **2018**, *95*, 43–56. [CrossRef]
30. Cai, Z.; Huang, Z.; He, M.; Li, C.; Qi, H.; Peng, J.; Zhou, F.; Zhang, C. Identification of Geographical Origins of Radix Paeoniae Alba Using Hyperspectral Imaging with Deep Learning-Based Fusion Approaches. *Food Chem.* **2023**, *422*, 136169. [CrossRef] [PubMed]
31. Xu, Y.; Ma, P.; Niu, Z.; Li, B.; Lv, Y.; Wei, S.; Hu, Y. Effects of Artificial Aging on Physiological Quality and Cell Ultrastructure of Maize (*Zea mays* L.). *Cereal Res. Commun.* **2023**, *51*, 615–626. [CrossRef]
32. Yin, G.; Xin, X.; Song, C.; Chen, X.; Zhang, J.; Wu, S.; Li, R.; Liu, X.; Lu, X. Activity Levels and Expression of Antioxidant Enzymes in the Ascorbate-Glutathione Cycle in Artificially Aged Rice Seed. *Plant Physiol. Biochem.* **2014**, *80*, 1–9. [CrossRef] [PubMed]
33. Zhang, M.; Li, P.; Dong, W.; Tang, S.; Wang, Y.; Li, R.; Ju, S.; Guan, B.; Zhu, J.; Kong, J.; et al. Identification of Hybrid Indica Paddy Rice Grain Varieties Based on Hyperspectral Imaging and Deep Learning. *Biosensors* **2025**, *15*, 647. [CrossRef] [PubMed]
34. Li, P.; Tang, S.; Chen, S.; Tian, X.; Zhong, N. Hyperspectral Imaging Combined with Convolutional Neural Network for Accurately Detecting Adulteration in Atlantic Salmon. *Food Control* **2023**, *147*, 109573. [CrossRef]
35. Wu, J.; Nie, J.; Hu, H.; Xu, X.; Li, C.; Zhou, H.; Feng, P.; Mei, H.; Rogers, K.M.; Wang, P.; et al. Characterizing Chinese Saffron Origin, Age and Grade Using VNlR Hyperspectral Imaging and Machine Learning. *Food Res. Int.* **2025**, *202*, 115585. [CrossRef] [PubMed]
36. Ambrose, A.; Kandpal, L.M.; Kim, M.S.; Lee, W.H.; Cho, B.K. High Speed Measurement of Corn Seed Viability Using Hyperspectral Imaging. *Infrared Phys. Technol.* **2016**, *75*, 173–179. [CrossRef]
37. Ribeiro, J.S.; Ferreira, M.M.C.; Salva, T.J.G. Chemometric Models for the Quantitative Descriptive Sensory Analysis of Arabica Coffee Beverages Using near Infrared Spectroscopy. *Talanta* **2011**, *83*, 1352–1358. [CrossRef] [PubMed]
38. Zhang, L.; Sun, H.; Rao, Z.; Ji, H. Hyperspectral Imaging Technology Combined with Deep Forest Model to Identify Frost-Damaged Rice Seeds. *Spectrochim. Acta A Mol. Biomol. Spectrosc.* **2020**, *229*, 117973. [CrossRef] [PubMed]

39. Wakholi, C.; Kandpal, L.M.; Lee, H.; Bae, H.; Park, E.; Kim, M.S.; Mo, C.; Lee, W.H.; Cho, B.K. Rapid Assessment of Corn Seed Viability Using Short Wave Infrared Line-Scan Hyperspectral Imaging and Chemometrics. *Sens. Actuators B Chem.* **2018**, *255*, 498–507. [CrossRef]
40. Fan, Y.; Liu, S.; Wang, Q.; Wang, Z.; Long, Y.; Chen, L.; Huang, W. Viability Discrimination and Vigor Estimation of Naturally Aged Open-Pollinated Maize Seeds via Hyperspectral Imaging. *Microchem. J.* **2026**, *221*, 116758. [CrossRef]

Disclaimer/Publisher's Note: The statements, opinions and data contained in all publications are solely those of the individual author(s) and contributor(s) and not of MDPI and/or the editor(s). MDPI and/or the editor(s) disclaim responsibility for any injury to people or property resulting from any ideas, methods, instructions or products referred to in the content.